Low Frequency Plasma Oscillations in a 6-kW Magnetically Shielded Hall Thruster

Benjamin A. Jorns* and Richard R. Hofer†

Jet Propulsion Laboratory, California Institute of Technology, Pasadena, CA 91109

The oscillations from 0-100 kHz in a 6-kW magnetically shielded thruster are experimentally characterized. Changes in plasma parameters that result from the magnetic shielding of Hall thrusters have the potential to significantly alter thruster transients. A detailed investigation of the resulting oscillations is necessary both for the purpose of determining the underlying physical processes governing time-dependent behavior in magnetically shielded thrusters as well as for improving thruster models. In this investigation, a high speed camera and a translating ion saturation probe are employed to examine the spatial extent and nature of oscillations from 0-100 kHz in the H6MS thruster. Two modes are identified at 8 kHz and 75-90 kHz. The low frequency mode is azimuthally uniform across the thruster face while the high frequency oscillation is concentrated close to the thruster centerline with an m = 1 azimuthal dependence. These experimental results are discussed in the context of wave theory as well as published observations from an unshielded variant of the H6MS thruster.

Nomenclature

$I_v(r,\theta,t)$	Light intensity at position (r,θ) and time t
$\overline{I}_v(r,\theta)$	Mean light intensity at position (r,θ)
$\mathcal{I}_v(r,\theta,t)$	Light intensity normalized by the mean value
$i_{sat}(r,t)$	Ion saturation current at radius r and fixed axial position
$\bar{i}_{sat}(r,t)$	Mean ion saturation current at radius r and fixed axial position
$\mathcal{I}_{sat}(r,t)$	Ion saturation current normalized by the mean value
$\mathcal{F}$	Fourier transform with respect to time
$P_{S(sat)}$	Power spectrum of normalized ion saturation current (r,θ)
$P_{S(v)}$	Power spectrum of normalized light intensity at position (r,θ)
$P^m_{S(v)}$	Power spectrum of normalized light intensity in azimuthal direction and time
N_b	Number of azimuthal bins
$\langle\mathcal{I}\rangle_{\bar{r},j}$	Azimuthally binned light intensity
ϕ_ω	Phase dependence of propagating modes
m	Azimuthal mode number
v_n	Neutral velocity
v_i	Ion exhaust velocity
L_i	Length of ionization zone
r_0	Density gradient lengthscale

*Associate Engineer, Electric Propulsion Group, 4800 Oak Grove Dr., M.S. 125-109, Pasadena, CA 91109. Member AIAA.
†Senior Engineer, Electric Propulsion Group, Associate Fellow AIAA.

ϕ_ω	Phase of mode at frequency ω
$\tilde{\phi}$	Amplitude of plasma potential oscillation
f_b	Breathing mode frequency
$n_{e,i}$	Electron, ion collision density
$\mathbf{v}_{e,i}$	Electron, ion species
$\nu_{e,i}$	Electron-neutral, ion-neutral collision frequency
$\tilde{\phi}$	Amplitude of potential oscillations
ω^*	Diamagnetic drift frequency
T_e	Electron temperature in units of energy
q	Fundamental charge
c_s	Ion sound speed
$m_{e,i}$	Electron, ion mass
k_z	Component of wavenumber in axial direction
$\mathbf{B}$	Magnetic field
z_c	Channel length measured from anode
r_c	Channel width

I. Introduction

With the advent of magnetically-shielded (MS) technology, the long-standing problem of erosion in Hall thruster channel walls has largely been solved.[1] This breakthrough was enabled by the observation of major reductions in channel erosion after a life test of Aerojet's BPT-4000[2] and the subsequent explanation at the Jet Propulsion Laboratory (JPL) of the basic physics that led to these reductions.[3] The derivation of the magnetic shielding first principles at JPL was followed by a validation program, which among other objectives, served to demonstrate these principles by testing a laboratory Hall thruster—the H6—after its magnetic field and channel geometry were modified from the original "unshielded" configuration.[4–6]

While as a consequence of these previous investigations the erosionless state that results from the modifications necessary to achieve magnetic shielding is now well-understood and established, the impact of the MS upgrade on the transients in the thruster remains unclear. This is an important, unresolved question in light of the potential effect oscillations have been proposed to have on Hall thruster processes such as cathode erosion[8–10] and anomalous transport.[11–18] Moreover, with new missions enabled by MS technology calling for higher specific impulse and power over longer timescales,[19] there is a pressing need for high-fidelity models for thruster performance. Our uncertainty about the underlying processes governing thruster oscillations limits our ability to self-consistently achieve this end as any accurate model must be supplemented with empirical scaling laws or periodic experimental measurements of the thruster in question. This reliance on empirical trends is common to all variations of Hall thrusters; however, it represents a particularly signficant challenge for MS technology where the database of experimental results and theory on oscillations is nascent.

In light of our need for high-fidelity models and our uncertainty concerning thruster transients, we present in this paper for the first time an experimental and analytical characterization of the oscillations in a magnetically shielded thruster. We choose to focus on the low-frequency range from 0 - 100 kHz as it has been shown experimentally to contain a number of modes in unshielded configurations—most notably the breathing mode[20–24] and rotating spokes[11,12,17,18]—that are believed to play a role in thruster stability and electron transport. In order to characterize these modes in an MS configuration, this paper is organized in the following way. In the first section, we outline the experimental setup and wave diagnostics. In the second section, we employ a series of analysis techniques to characterize both the global and local character of oscillations in the thruster. In the third section, we attempt to categorize the observed modes through an analytical treatment and a direct comparison with measurements reported for an unshielded thruster. In the

fourth and final section, we summarize our findings and discuss the implications for future efforts to model oscillations in MS thrusters.

II. Experimental Setup

The goal of this experimental investigation was to employ a set of diagnostics to characterize oscillations in the near plume of a MS Hall thruster. In the following section, we present descriptions of the facility and thruster as well as the two primary diagnostics we employed: a translating ion saturation probe and a high speed camera.

A. Facility

We performed all of the experimental trials reported here in the Owens Chamber located at the Jet Propulsion Laboratory. This facility, formerly known as the Endurance Test Facility, is a 3 m $\times$ 10 m cylindrical vacuum chamber cryogenically-pumped to a steady-state background pressure of 5×10^{-7} Torr. At the 20 mg/s flow rate of Xenon employed in this set of trials, we measured the background pressure at $P_B = 1.4 \times 10^{-5}$ Torr, which indicates a total pumping speed of 180 kl/s at the standard temperature of 0° C .

B. H6 Hall Thruster

For this set of trials, we characterized the oscillations in the H6MS,[4–6] a magnetically-shielded 6-kW thruster Hall thruster (Fig. 1). This thruster is a modification of the original baseline configuration H6US, which was the result of a joint development between the Air Force Research Laboratory, JPL, and the University of Michigan. The H6US has been thoroughly investigated experimentally and noted for its high performance and reliability.[25–30]

While the H6MS and H6US share many of the same physical characteristics including the same anode and a custom, lanthanum hexaboride, center-line mounted cathode,[31] the magnetically shielded configuration varies from the baseline configuration primarily through a change of the magnetic field topography. The consequence of this modification is that the plasma at the channel walls is maintained close to the anode potential and with a low electron temperature. This yields a steady state where resultant electric fields at the walls significantly inhibit energetic ion flux and thus effectively eliminate erosion.[1]

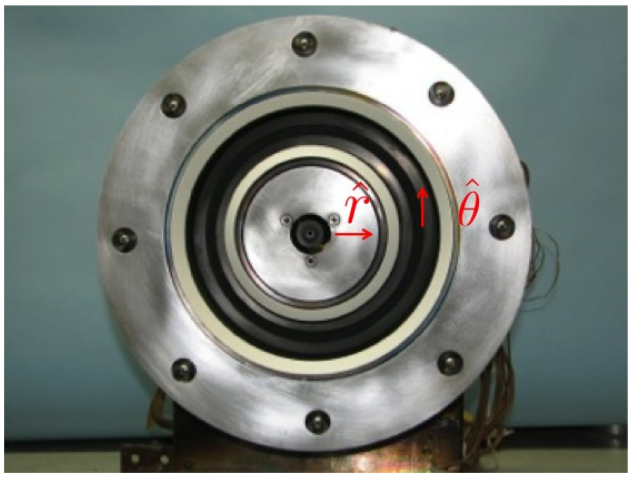

Figure 1. H6MS with new boron nitride rings and labeled directions. The axial direction is directed outward from the thruster face.

As can be seen from Fig. 2, a side-effect of the modification to the magnetic field topography to achieve the MS effect is a shift of the region of maximum magnetic field, electric field, and temperature to a position downstream as compared to the baseline configuration. This shift is accompanied by slight changes in the characteristic lengths of these plasma parameter profiles. As both wall interactions and plasma gradients have been identified as potential drivers for low-frequency oscillations in Hall thrusters,[12,22,32–36] it is reasonable to expect these changes may result in significant differences in the oscillation spectrum of MS thrusters.

The study of the H6MS is an expedient choice for identifying these differences as the unshielded variation of the thruster, the H6US, has been the subject of an extensive study of low-frequency oscillations.[17,37–41] By running the H6MS at the same operating point as the H6US, we are able to make a direct comparison between the two implementations.

For this set of trials, we ran the H6MS at the nominal condition of 300 V and a flow rate of 20 mg/s of research-grade xenon with a flow split to the center-mounted cathode of 7%. At this operating condition, the thruster is thermally and operationally stable with a thrust of 384 mN, a specific impulse at 2000s, and an efficiency of 62.4%.[5] These values are all within 5% of the operating conditions reported for the H6US under similar operating conditions. Two power supplies connected in parallel provided the current and voltage drop to the thruster. A 80 μF shunt capacitor served the dual purpose of protecting the power supplies while minimizing the role of power supply driven oscillations in our experimental characterization.

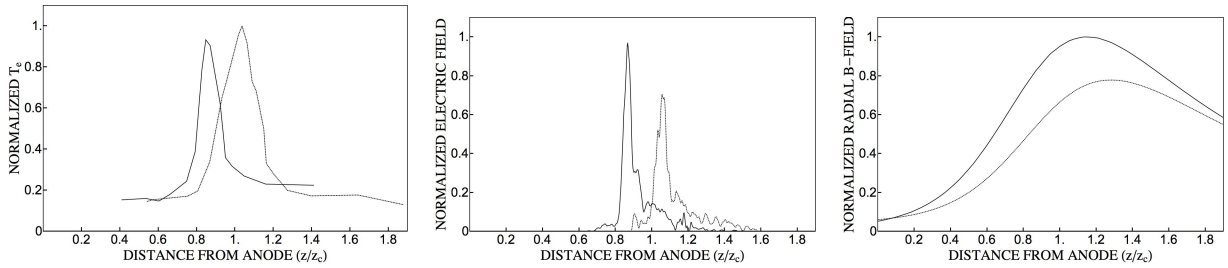

Figure 2. Electron temperature, electric field, and magnetic field for the H6US (solid line) and H6MS (dashed line) along the channel centerline as functions of position. Adapted from results presented in Ref. 5.

C. High Speed Imaging

In recent years, an increasing precedent has evolved for the use of high speed imaging to characterize fluctuations in the channels and near-field plumes of Hall thrusters.[17,18,42–44] By rendering black and white images from a view downstream of the thruster, high speed imaging yields measurements of variations in light intensity that happen on a time scale slower than the frame rate of the camera. This permits a noninvasive assessment of the spatial and time dependent fluctuations at the thruster face and inside the channel. For our implementation of this technique with the H6MS in the Owens chamber, we employed a FASTcam SA1 built by Phototron. We show a qualitative schematic of the camera and its layout with respect to the experimental chamber in Fig. 3. The location of a beam dump in the immediate region downstream of the H6MS prevented a direct, on-axis positioning of the FASTcam diagnostic. However, an off-center window permitted a near axial interrogation of the thruster configuration at $\sim 5^\circ$

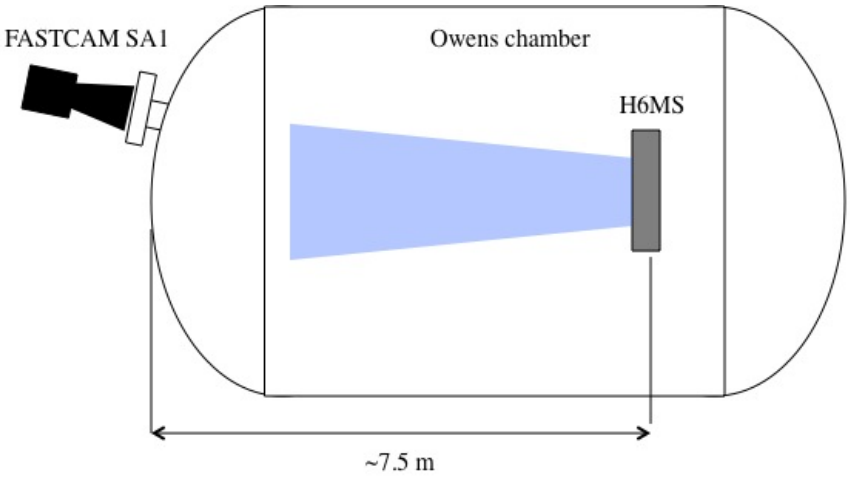

Figure 3. Diagram of the FASTcam SA1 setup in the Owens Chamber.

In order to capture the high frequency oscillations at $\sim$ 80 kHz that have been reported in the H6MS configuration,[5] we operated our camera at the high frame rate of 180 kHz—yielding a Nyquist cutoff of 95 kHz and a pixel resolution of 128 x 128. As a compromise between the reduced light intensity at this high sampling rate and the need to maximize spatial resolution of the thruster face, we employed a 35 mm lens with a 2 aperture. The thruster face consequently occupied 100 pixels of the available 128 pixels. This resolution is half of that reported for the H6US characterization[37,38] where a lower frame rate and a more sophisticated version of the FASTcam were employed. The bit depth of all images was 16, and we were careful to never allow the cathode to saturate the image. This would have precluded an investigation of the fluctuations in this region. A sample raw image from the FASTcam is shown in Fig. 4.

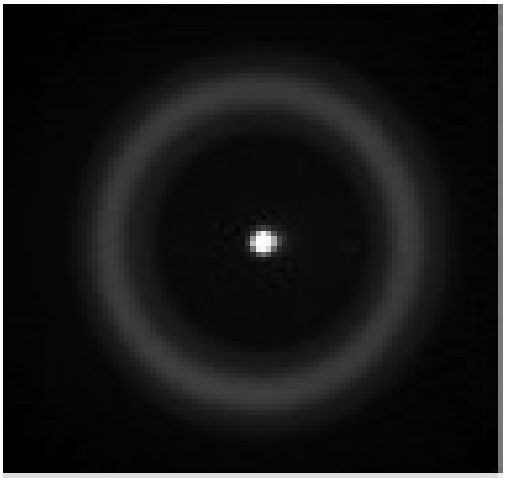

Figure 4. Raw image from one frame taken with the FASTcam SA1 at 180 kfps. The channel and cathode are clearly visible. While the cathode intensity dominates the image, it did not saturate the camera range.

D. Translating Ion Saturation Probe

In order to augment the FASTcam analysis of the fluctuations in the near-field plume of the thruster, we employed a single, negatively-biased cylindrical Langmuir probe capable of translation in the radial direction. This probe provided a direct, local measurement of ion saturation fluctuations.

We performed radial scans with the probe at an axial position one channel length, z_c, downstream of the pole piece. Each scan consisted of twenty points over the radial range from $0.65 < r/r_c < 2.5$, where r_c is the channel width. The probe would stop at each point, scan for approximately three seconds, and move to the next point. While we selected this long time interval to increase the signal to noise ratio of the power spectra with real-time averaging, it also resulted in a long resident time in the plasma—exposing the probe and housing structure to significant bombardment. This was particularly problematic near the cathode where we had observed placing the probe in this vicinity for an extended period of time would disrupt thruster operation. We therefore defined the scan to end outside the cathode region. As a result, while the ion saturation probe provided useful information on oscillations in the channel, we could not use it to augment our FASTcam analysis near the centerline cathode.

III. Experimental Results

In this section, we present the measurements of the oscillations in the H6MS that we performed with the diagnostics outlined above. These results reflect oscillations in the thruster after it had reached equilibrium at the nominal conditions of 300 V and 20 A. The following discussion consists of an analysis of three data sets for this operating point: 8000 FASTcam images taken at a frame rate of 180 kps, traces of the thruster discharge current that were triggered to be taken simultaneously with the camera shots, and the frequency content of a radially translated ion saturation probe.

A. Global analys

As an initial check of the thruster oscillations, we first want to characterize the the global behavior of the light intensity. To this end, let us denote the local intensity of a single frame from the FASTcam at time t and at position (r, θ) as $I_v(r, \theta, t)$. We thus see that the normalized total intensity of each image as a function of time is given by

$$\langle \tilde{\mathcal{I}}_v \rangle_A = \frac{\langle I_v(r,\theta,t) \rangle_A - \langle \bar{I}_v(r,\theta,t) \rangle_A}{\langle \bar{I}_v(r,\theta,t) \rangle_A}, \tag{1}$$

where $\langle .. \rangle_A$ denotes the spatial average over the thruster face and $\bar{I}_v$ is the average with respect to time. We show this quantity in Fig. 5 compared to the normalized fluctuations in the discharge current, $\mathcal{I}_D = \tilde{I}_D / \bar{I}_D$ measured over the same time period. We can see that without any additional correction to phase or vertical scaling, the amplitudes of the two signals correspond almost exactly. This result suggests that the global fluctuations in intensity, normalized by the mean, are an excellent proxy for the fluctuations in discharge current. A similar observation is found for the unshielded configuration.[41]

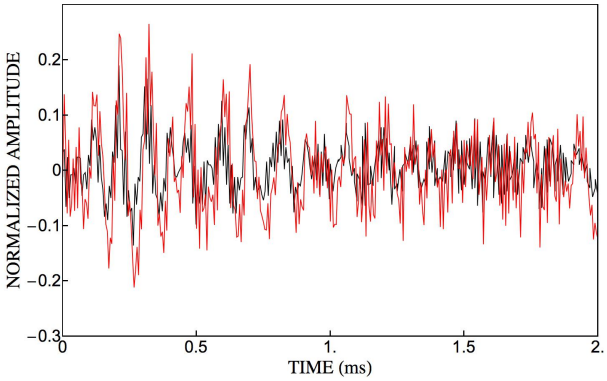

Figure 5. Fluctuations in discharge current (black) and the total light intensity (red) normalized by the time-averaged values.

We can confirm the correspondence between discharge current and global light intensity explicitly with an analysis of the power spectra of the two signals that we show in Fig. 6. It is evident from these plots that the power spectra of the normalized oscillations yield similar amplitudes and the same qualitative character as a function of frequency. In particular, they exhibit two distinct features: a dominant mode at 8 kHz and a higher frequency mode from 70 - 95 kHz.

We thus find the reasonable result that the global oscillations in the light intensity directly reflect changes in the global, spatially-averaged current conducted by the thruster. In the following sections, we attempt to determine the origin of the peaks in these global metrics as well as the existence of spatially-non uniform modes that may have been averaged out in the above treatment.

B. Spatial dependence of frequency spectrum

While the global analysis of the fluctuations in total intensity give us insight into the impact of average plasma parameters on discharge current, spatial averaging precludes us from examining the local character of the fluctuations in the Hall thruster. Are the oscillations we identified at 75-90 kHz and 8 kHz spatially uniform? Are there non-spatially uniform oscillations that have been averaged with this procedure? In order to address these questions, we now examine the following parameter:

$$P_{S(v)} = \left| \mathcal{F}\left[\tilde{\mathcal{I}}_v(r,\theta,t) \right] \right|^2, \tag{2}$$

where we have defined $\tilde{\mathcal{I}}_v(r,\theta,t) = I_v(r,\theta,t) / \bar{I}_v(r,\theta)$, $\mathcal{F}$ denotes the Fourier transform with respect to time, and $|..|$ is the magnitude of the complex quantity. This parameter is a measure of spatial dependence of the power spectrum of the normalized light intensity signal where the normalizing term is the time-averaged light intensity at a given position. This normalization scheme results in a term that is quadratically proportional to

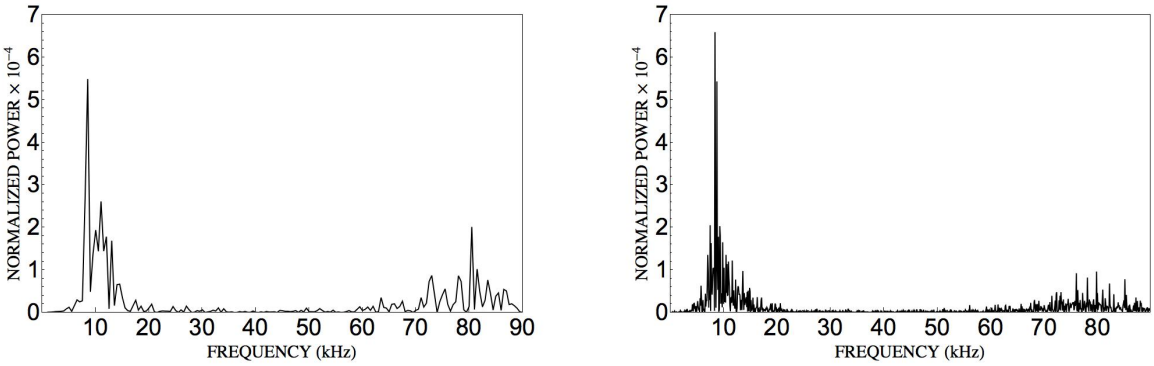

Figure 6. Left: Power spectrum of fluctuations in the normalized discharge current. Right: Power spectrum of the normalized and integrated light intensity. The upper bound on frequency is dictated by the Nyquist criterion of the FASTcam (95 kHz).

the local fractional change in light intensity. We employ this normalization metric throughout this discussion since it controls for the fact that there is a great degree in disparity in light intensity between different regions of the Hall thruster face.

With this in mind, we show $P_{S(v)}$ at a fixed angle and as a function of radius and frequency to the left of Fig. 7. From this plot, we immediately can see the local features of the fluctuations in light intensity. Most notably, while the low frequency mode persists across the thruster face and the channel, the high frequency content at 75-90 kHz is localized near the center-mounted cathode. Moreover, the fractional change in light intensity at this region is significantly larger than observed with the low frequency oscillations anywhere else at the thruster face. The fact that the greatest peak over the whole thruster occurs in the range 75-90 kHz can be reconciled with the fact that the greatest peak occurs at 8 kHz in the spatially averaged plot in Fig 6 by considering that although the local peak is smaller at 8 kHz in Fig. 7, this feature is observed over almost the entire thruster face (as evidenced by the vertical line). The 75-90 kHz signal, however, is localized in the immediate vicinity of the cathode. Therefore, when integrating over the thruster face to produce the spatial average, the total magnitude of the 8 kHz signal becomes dominant.

Additionally, while we clearly can resolve the two frequency peaks in this figure, there are no other apparent regions where other frequency content is exhibited. In other words, although it is possible that our averaging procedure from the previous section may have eliminated spatially dependent modes at frequencies other than the two predominant ones exhibited in the discharge current power spectrum, the localized plot in Fig. 7 illustrates that if any such modes are present, their relative amplitudes are at least two orders of magnitude smaller than those exhibited here.

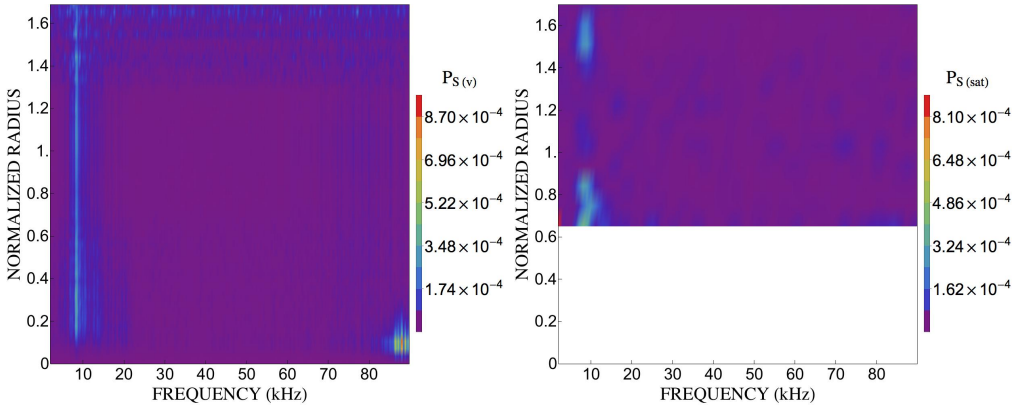

Figure 7. Left: the local power spectrum of the normalized light intensity as a function of thruster radius and frequency. Right: the local power spectrum of the normalized ion saturation current density at axial position $z = z_c$ distance from the thruster face and as a function of thruster radius. The radius in both cases has been normalized by the distance from the thruster centerline to the centerline of the channel, r_c.

Of course, we recognize that while light intensity may serve as a good proxy for global plasma parameters (as demonstrated in the previous section), the local fluctuations in light intensity as measured by the camera may not be representative of the actual variations in plasma parameters at the thruster face. This in part stems from the fact that the light intensity signal is necessarily an integration of the light along the entire path length from the thruster to the camera. As a check for our local analysis of the thruster face then, we employed the translating ion saturation probe outlined in Sec. II.D to examine the normalized variations in ion saturation as a function of radius:

$$\tilde{\mathcal{I}}_{sat}\left(r,t\right)=\frac{i_{sat}\left(r,t\right)}{\bar{i}_{sat}\left(r\right)}, \tag{3}$$

where i_{sat} denotes the ion saturation current and $\bar{i}_{sat}$ is the time-averaged ion saturation current. This is a physically meaningful parameter under the assumption of constant local electron temperature as it corresponds to $\tilde{\mathcal{I}}_{sat}\left(r,t\right)=\tilde{n}_i/\overline{n}_i$ where n_i denotes the ion density.

We plot the power spectrum of $\tilde{\mathcal{I}}_{sat}$ as a function of radius and at axial position $z=z_c$ on the right of Fig. 7. It is evident from this plot that although we cannot measure the fluctuations immediately near the cathode with this method (due to the constraints outlined in Sec.D), the figure does exhibit two of the same qualitative trends as the intensity power spectrum: no transients appear outside the two peaks we have previously identified and the normalized amplitude of the lower frequency persists across the thruster face. We thus use this additional diagnostic first to confirm that over the region we interrogated with the probe that the variations in light intensity do reflect local variations in plasma parameters and second to conclude that there are no detectable local modes in the near-field plume outside the two already identified ranges. We are prevented from drawing the same conclusions linking imaging results from the FASTcam and probe measurements near the thruster centerline due to the missing data; however, in light of the fact that plasma density is highest at the cathode and—in contrast to channel oscillations— there is no significant source of light intensity behind the region at the cathode, we proceed under the assumption that light intensity fluctuations near the centerline do reflect local variations in plasma parameters axially close to the thruster face.

With this in mind, as a final characterization of the spatial dependence of the two dominant modes, we examine the amplitudes at these frequencies as a function of radius. Returning to the FASTcam data, we calculate the integrated quantities at a fixed angle

$$P_{s(v)}^{LF}\left(r\right)=\int_{f=7\text{ kHz}}^{f=9\text{ kHz}}P_{s(v)}\left(r,0\right)d\omega \tag{4}$$

$$P_{s(v)}^{HF}\left(r\right)=\int_{f=75\text{ kHz}}^{f=90\text{ kHz}}P_{s(v)}\left(r,0\right)d\omega. \tag{5}$$

These terms provide a measure of the square of the amplitudes of the modes propagating in the indicated frequency ranges. We show these calculated expressions in Fig. 8 as a function of position where we have normalized the profiles to the peak value exhibited by the 75-90 kHz trace. For comparison, we also plot the mean light intensity $\overline{I}_v\left(r,0\right)$ as a function of radius. It is evident from this figure that the fractional change in light intensity for the lower amplitude mode is relatively constant across the thruster face but goes to zero at the centerline. The amplitude of the 75-90 kHz mode, however, goes to zero at the centerline and exhibits an off-center peak. Interpreting the light intensity as a proxy for variations in plasma density, this radial dependence of the higher frequency oscillation suggests that it may be a radial eigenmode. We explore this interpretation further in Sec. IV.B.

With these results, we now have established that the low frequency modes have a global character and the high frequency modes are highly localized. In the next section, we explore the spatial dependence of both modes in the azimuthal direction.

C. Azimuthal dependence of propagating modes

In order to isolate and characterize the azimuthal dependence of the fluctuations in normalized light intensity, we need to determine the power spectra in both time and the azimuthal direction. This, in principle, allows us to identify the azimuthal mode number of the oscillation at frequency ω and at radial position r. However, while a direct Fourier analysis in the azimuthal direction provides the highest spatial resolution in the radial

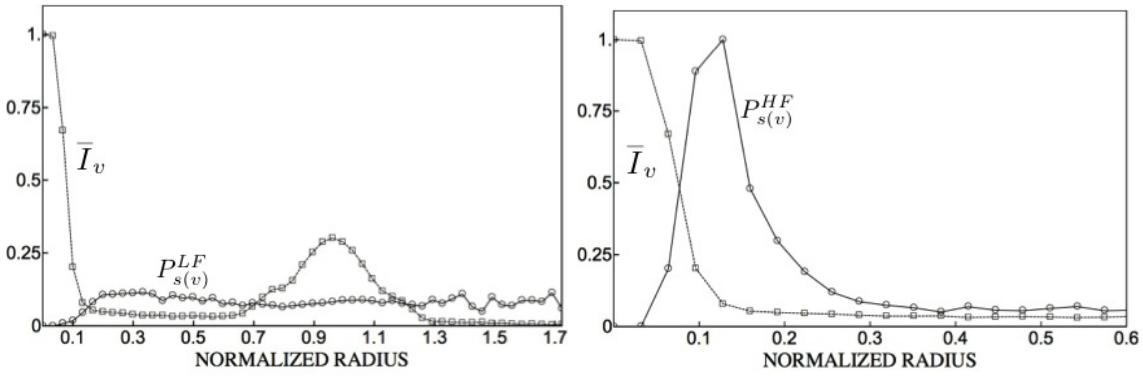

Figure 8. Left: The square of the amplitude of the normalized oscillation in light intensity over the frequency range 7 - 9 kHz as a function of radius (open squares) plotted versus the mean light intensity as a function of radial position (open circle). Right: The same convention applies but over the frequency range 75-90 kHz. The oscillation amplitudes have been normalized to the maximum that occurs in the right hand side. The mean intensity profiles have been normalized to the maximum at $r = 0$.

direction, in light of the discrete nature of the pixelated images provided by the FASTcam and in the interest of increasing the signal to noise ratio, we forgo this metric in favor of the azimuthal binning technique outlined by McDonald and Gallimore.[37,38]

To this end, we begin by selecting a range of values in radius $r_{min} < r < r_{max}$ and a number of bins N_b in the azimuthal direction such that the θ coordinate is discretized: $\theta_j = j2\pi/N_b$ where $j = 0..N_b - 1$. We then denote the averaged quantity

$$\langle \mathcal{I}_v \rangle_{\bar{r},j} = \frac{N_b}{8\pi \bar{r} \Delta r} \int_{r_{min}}^{r_{max}} \int_{\theta_j}^{\theta_{j+1}} \mathcal{I}_v\left(r, \theta, t\right) r dr d\theta, \tag{6}$$

where we have $\Delta r = r_{max} - r_{min}$ and $\bar{r} = \Delta r/2$. Implementing Fourier transforms in both space and time to this binned data yields

$$P^m_{S(v)}\left(\bar{r}, \omega\right) = \frac{2}{N_b} \left| \sum_{j=1}^{N_b} \mathcal{F}\left[\mathcal{I}_v\left(r, \theta, t\right)\right] e^{-im\theta_j} \right|^2. \tag{7}$$

With this metric, we have plotted in Fig. 9 the azimuthal modes as a function of frequency in the channel ($0.8 < r/r_c < 1.2$) and near the cathode ($0 < r/r_c < 0.13$). The channel plots consist of $N_B = 180$ bins while near the cathode, in order to compensate for the limited pixel resolution, we set $N_B = 45$.

From the lefthand side Fig. 9, we immediately can see that there are no coherent modes in the azimuthal direction in the channel. Indeed, by comparing the amplitudes from Fig. 7 at this radius and the plot in Fig. 9 over the same radii, it is evident that all of the power is concentrated in $m = 0$ oscillations and that these oscillations are dominated by the lower frequency mode at 8 kHz. All other content is at least two orders of magnitude smaller. Interestingly, we note that a significant frequency component does appear at 75-90 kHz, though this content also has no azimuthal character. On the other hand, as exhibited by the second plot in Fig. 9, we note that near the cathode, the power spectra are dominated by a high frequency $m = 1$ mode with a small amount of spectral bleeding into higher order modes. At the average radius $\bar{r} = 0.065$, this figure indicates the $m = 1$ mode is propagating with an azimuthal speed of 4.2 km/s. We also note—as indicated by Fig 7—that the low frequency $m = 0$ mode persists at least in part of the interrogated region.

The structure of the two dominant modes thus becomes more clear. By employing an azimuthal binning technique over specified ranges of radius, we have explicitly examined the azimuthal character of the modes near the channel and the cathode, and we have determined that the former is uniform while latter has an $m = 1$ character. With this knowledge and our assertion from Sec. III.B that at least one of the oscillations has a radial character, we now turn in the next section to an attempt to visualize the propagation of modes in both the radial and azimuthal directions concurrently.

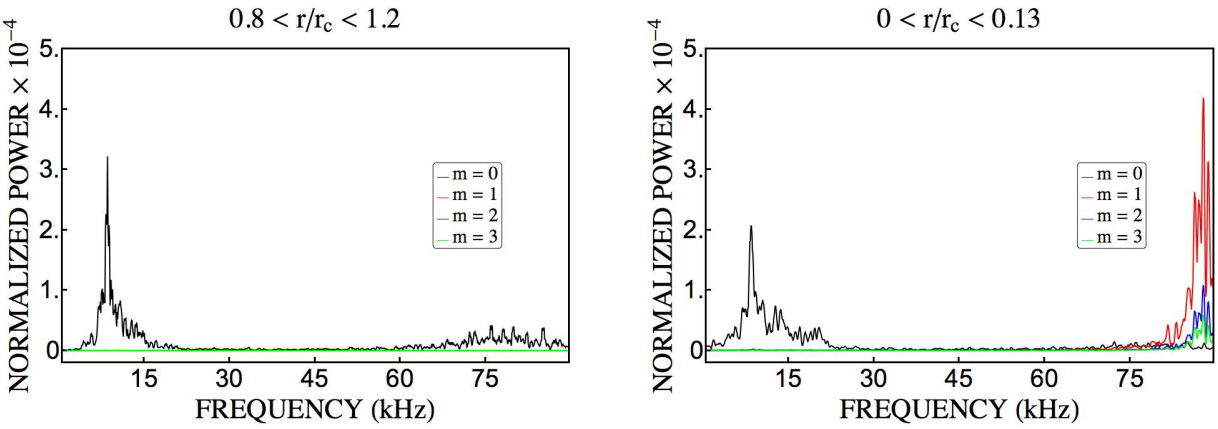

Figure 9. Power spectra for $m = 0, 1, 2, 3$ azimuthal modes. Left: the radial average is over the channel width. Right: the radial average is over the area near the cathode where the 75-90 kHz oscillations are dominant.

D. Phase dependence of the propagating modes

With the knowledge of the frequency ranges to investigate (Fig. 7) and the azimuthal dependence of each type of oscillation (Fig. 9), we now are in the position to characterize in two dimensions the waves in the thruster. To motivate the method for achieving this end, we first consider the following simple model for azimuthally and radially propagating waves in a cylindrical geometry:

$$\tilde{n} \sim \sum_{\omega} e^{i\left(m_\omega \theta + k_{r(\omega)} r - \omega t\right)}, \tag{8}$$

where $k_{r(\omega)}$ denotes the wave vector in the radial direction and we have summed over all the frequency components. The phase of the mode at frequency ω is defined as $\phi_\omega(r,\theta) = m_\omega \theta + k_{r(\omega)} r$, and it is this quantity that provides a means for us to characterize the spatial content of the mode in two dimensions. For example, by plotting ϕ_ω as a function of position in two-dimensions, an $m = 1$ is revealed by a 2π periodicity in θ. Similarly, radial propagation is characterized by variations in ϕ_ω as a function of r.

To translate this example to the FASTcam data from the H6MS, we note that the intensity at a given position in the thruster is a continuous superposition of frequency components

$$\mathcal{I}_v(r,\theta,t) = \frac{1}{2\pi} \int_{-\infty}^{\infty} \left|\mathcal{F}\left[\mathcal{I}_v(r,\theta,t)\right]\right| e^{i(\phi_\omega(r,\theta) - \omega t)} d\omega, \tag{9}$$

where we recall that the magnitude of the Fourier transform is a function of the frequency. In order to find the phase ϕ_ω as a function of position from this formulation, we consider the normalized light intensity at two points, $\mathcal{I}_v(r_0,\theta_0,t)$, and $\mathcal{I}(r,\theta,t)$. Fourier transforming Eq. 9 at these two positions with respect to time, we can manipulate the measured quantities to find the phase difference

$$\Delta\phi_\omega = \phi_\omega(r,\theta) - \phi_\omega(r_0,\theta_0) = \tan^{-1}\left[\frac{\mathrm{Im}\left(\mathcal{F}^*\left[\mathcal{I}_v(r_0,\theta_0,t)\right]\mathcal{F}\left[\mathcal{I}_v(r,\theta,t)\right]\right)}{\mathrm{Re}\left(\mathcal{F}^*\left[\mathcal{I}_v(r_0,\theta_0,t)\right]\mathcal{F}\left[\mathcal{I}_v(r,\theta,t)\right]\right)}\right], \tag{10}$$

where $\mathcal{F}^*$ denotes the complex conjugate. By allowing (r_0,θ_0) to be fixed, we can use this prescription to map out the phase dependence of the intensity at the frequency ω as a function of position. We note here that this method has the additional advantage—as can be seen from Eq. 10—that the magnitude of the light

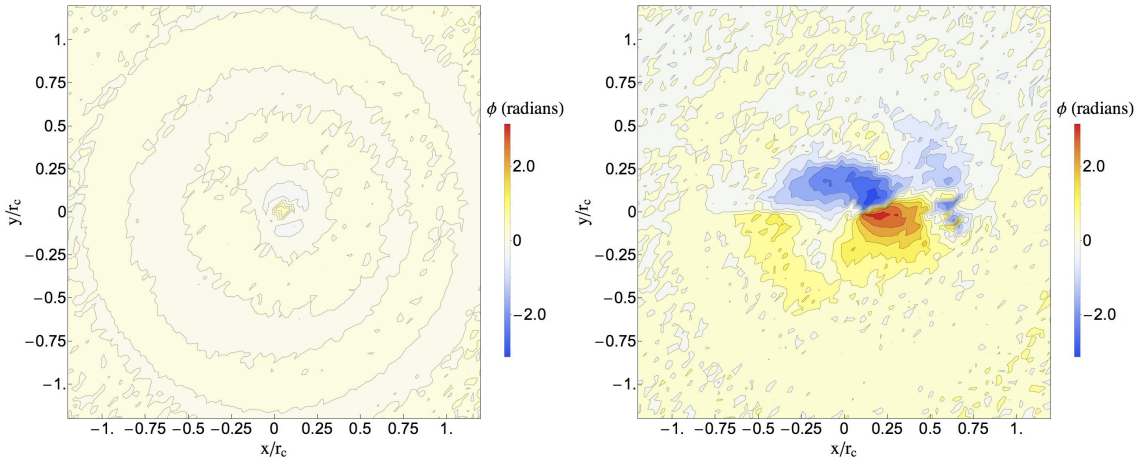

Figure 10. Left: phase of the mode at 7 - 9 kHz as a function of position. The reference point (r_0, θ_0) we employed to generate this plot is located in the channel. Right: Phase of the mode at 75 - 90 kHz as a function of position. The reference point (r_0, θ_0) to generate this plot is located off-axis and close to the cathode.

intensity is removed in this calculation of phase. This permits us to examine the phase dependence even over regions where this is a large disparity in signal light intensity.

Employing this metric, we have plotted the phase dependence of the dominant modes at 8 kHz and 75-90 kHz in Fig. 10. We generated these plots by calculating $\phi_\omega(r, \theta)$ for the entire frequency spectrum according to the prescription from Eq. 10. We then averaged ϕ_ω over the frequency ranges of interest exhibited by the power spectra in Fig. 9— 7–9 kHz and 75 - 90 kHz. The reference point we used to calculate the component of Eq. 10 at (r_0, θ_0) in the 8 kHz plot was in the channel while the reference point was slightly off the centerline for the 75-90 kHz plot. The color on each figure indicates the phase angle—in the range between $(-\pi, \pi)$.

The first plot in Fig. 10 exhibits the phase dependence of the low-frequency mode. We now can see that our observation from the previous section that this mode is azimuthally uniform $(m = 0)$ is borne out. Almost the entire thruster is in phase with $|\phi_\omega| < 0.3$. In other words, this correlation analysis reveals that at 8 kHz, the entire thruster face oscillates uniformly with no azimuthal character. There are slight deviations in phase as a function of radius, but the change is too small to suggest significant radial propagation. On the other hand, the second plot in Fig. 10 reveals the distinct character of the $m = 1$ mode we identified in the previous section. Indeed, it is evident from the variation in phase that not only does this mode propagate in the clockwise direction but it has a distinctive swirl to it. This latter feature is an indication that there is a component of propagation directed radially-outward from the centerline.

In sum, through a combination of local power spectra analysis and correlation techniques, we can draw the following conclusions from our experimental analysis. There are two distinct oscillations in the normalized light intensity in the frequency range from 0 - 100 kHz. One occurs at 8 kHz and oscillates globally across the thruster face. The other occurs at 75-80 KHz, exhibits a distinct spatial dependence in phase, and is confined close to the thruster centerline. Signficnatly, outside these two dominant modes, there are no other experimentally observed coherent oscillations. We discuss this result in the next section along with the nature of the two detected waves.

IV. Discussion

With the experimental characterization of the propagating modes from 0 - 100 kHz, we now are in a position to discuss the nature of these observations. To this end, we attempt to identify the observed modes in the context of previous investigations, the extensive observations of oscillations reported for the unshielded configuration H6US,[17,37,38] and a simple two-fluid model for the high frequency mode that we motivate here.

A. Breathing mode

From the observations in Sec. III, we briefly summarize the characteristics of the fluctuations in the normalized light intensity at 8 kHz:

- No azimuthal dependence (m = 0).
- Uniform phase across the entire thruster face.
- Nearly uniform amplitude across the thruster face with a small peak near the channel.
- Dominant contributor to oscillations in the total discharge current and light intensity.

These observations taken together suggest that this mode is the breathing mode oscillation,[21–24] an azimuthally uniform ionization wave with primarily axial propagation. The breathing mode is nearly omnipresent in Hall thrusters, and it is unsurprising that we find it in the MS configuration. Indeed, while the change in the magnetic field that results from the MS configuration does shift the ionization region downstream compared to traditional implementations of Hall thrusters (Fig. 2), the change does not significantly change the character of the ionization region. The underlying physical processes governing ionization and neutral propagation that lead to the growth of the breathing mode therefore are unchanged.

We do note, however, the interesting result that although the baseline configuration of the H6MS operated with the same performance parameters as the unshielded H6US, there is a discrepancy in the frequency of this mode: 14 kHz for H6US versus the 8 kHz we observe here. A possible explanation for this discrepancy may in part be explained in the context of the simplified model for breathing oscillations derived by Barral et al[45,46] , who found the same scaling as the simple but non self-consistent predator-prey model originally put forward by Fife et al:[47]

$$f_b = \mathcal{O}\left[\frac{\sqrt{v_n v_i}}{L_i}\right], \tag{11}$$

where v_n is the ion exhaust velocity, v_i is the ion drift velocity, and L_i is the length of the acceleration channel. Between the two configuration of the US and MS, the ion velocities and neutral velocities are equal. Therefore, the ratio between breathing mode oscillations scales as

$$\frac{f_{b(MS)}}{f_{b(US)}} = \frac{L_{i(US)}}{L_{i(MS)}}. \tag{12}$$

This expression indicates that the discrepancy between the frequencies in the two configurations could be explained by a difference in characteristic ionization lengths. In light of the results from Ref. 5 and Fig. 2, we can see that the change in magnetic contour for the MS configuration leads to a shift of the acceleration zone downstream. Since ionization begins at the anode, this simple scaling suggests a longer ionization length for the MS configuration, and indeed by assuming the ionization zone is proportional to the distance from the anode to the region of peak electric field, we find an estimate for the ratio as $L_{i(US)}/L_{i(MS)} \approx 0.8$. This ratio is too large to explain the observed shift frequency ratio of 0.57, but in light of the simplicity of the 1-D assumptions leading to Eq. 11, it does serve as an indication that the discrepancy may in large part be explained by an extended ionization zone in the MS configuration that results from a shift in the location of the peak magnetic field. A fully numerical model could better elucidate the underlying cause for the difference in frequencies.

B. Oscillations near the cathode

While a number of azimuthal oscillations in the 10-100 kHz ranges have been identified in unshielded Hall thruster (c.f. Ref. 24), these modes were observed primarily in the thruster channel where the plasma and field parameters are significantly different than those exhibited near the centerline cathode of the H6MS. This suggests that the oscillations near the cathode we observed are not related to previously reported modes. In an attempt to identify the nature of our highly-localized oscillations then, we proceed first by summarizing our observations of its properties and then examining theoretically the waves that can be driven unstable by the background plasma parameters in this region.

To this end, we have found the following properties for the fluctuations in the normalized light intensity in the 70 - 95 kHz range:

- The oscillation has an azimuthal $m = 1$ character propagating in the clockwise direction.
- There is a radial component of propagation.
- $\Omega_i < \omega < \Omega_e$ and $\omega < \omega_{pe}, \omega_{pi}$ where $\Omega_{i,e}$ denotes the cyclotron frequency and $\omega_{pe,pi}$ denotes the plasma frequency.

For the background plasma parameters, we assume that the oscillation is axially close to the pole piece and is subject to the plasma conditions near the cathode centerline ($0 < r/r_c < 0.13$). This yields the following observations, which we assembled from measurements of the H6MS magnetic field, the imaging data reported above, and the simulations of the H6MS performed in Refs. 4–6 with the two-fluid code, Hall2De:

- There is a strong density gradient from the centerline (Fig. 8).
- There is a small potential drop toward the centerline.
- The temperature is relatively constant at $T_e \approx 2$ eV.
- The magnetic field is axial and approximately uniform in this region.

The azimuthal propagation of the mode in the presence of a strong density gradient and electric suggests that the mode is a form of either shear-driven or gradient-driven instability. Such modes can occur at frequencies higher than the ion cyclotron frequency and can be further destabilized by the presence of an electric field.[35,36] Armed with the observations we have outlined above, we can examine the possibility of the gradient-driven nature of this mode more closely with a simple two-fluid model. To this end, we have referred to Ref. 48 for a two-fluid description in cylindrical coordinates:

$$0 = \frac{\partial n_\alpha}{\partial t} + \nabla \cdot n_\alpha \mathbf{v}_\alpha \tag{13}$$

$$n_\alpha m_\alpha \frac{d\mathbf{v}_\alpha}{dt} = -T_\alpha \nabla n_\alpha + q_\alpha n_\alpha \left(\mathbf{E} + \mathbf{v} \times \mathbf{B}_0\right) - m_\alpha n_\alpha \nu_\alpha \mathbf{v}_\alpha, \tag{14}$$

where m_α is the ion species mass, T_α is the species temperature, n_α is the species density, $\mathbf{v}_\alpha$ is the species velocity, and ν_α is the particle-neutral collision frequency. We then invoke a linearization of the quantities: $n = n_0 + \tilde{n}, \mathbf{E} = \mathbf{E}_0 + \tilde{\mathbf{E}}$, $\mathbf{v} = \mathbf{v}_0 + \tilde{\mathbf{v}}$ where we have

$$\tilde{n}, \tilde{\mathbf{E}}, \tilde{\mathbf{v}} \sim \tilde{\psi}\left(r\right) e^{i(m\theta - k_z z)}. \tag{15}$$

Here k_z denotes the parallel wave vector and $\tilde{\psi}(r)$ is a function of r. We now make the following approximations consistent with the observed mode and plasma parameters:

1. $\Omega_e \gg \nu_e$
2. The fluctuations are electrostatic, $\mathbf{E} = -\nabla\tilde{\phi}$, where $\tilde{\phi}$ denotes the wave potential amplitude.
3. The fluctuations are quasineutral, $\tilde{n}_e = \tilde{n}_i$.
4. The magnetic field is axial and uniform in the vicinity of the cathode face, i.e. $\mathbf{B}_0 = B_0\hat{z}$
5. The background plasma density has a radial gradient, $n_0 \sim e^{-r^2/r_0^2}$ but can be approximated as axially uniform in the vicinity near the cathode.
6. The ions are cold, $T_i \to 0$.
7. The mode is primarily azimuthal with a long wavelength in the parallel direction such that $\omega/k_z \gg c_s$ where $c_s = \sqrt{qT_e/m_i}$ denotes the ion sound speed.
8. The waves are weakly damped with respect to ion collisions but rendered unstable by the electron collisions, $\nu_i < \omega < \nu_e$.
9. The wave frequency is in between cyclotron frequencies $\Omega_i < \omega < \Omega_e$.
10. We can neglect electron inertia and ion acceleration.

11. The electrons drift in the axial direction with velocity u_0.

12. The ions have negligible zeroth order velocity.

13. We can neglect the electric field in the radial direction.

14. Electron temperature is constant over the region of interest.

Subject to these constraints, we can linearize Eq. 14 with Eq. 15 to find the zeroth order electron drifts given by

$$\begin{aligned} v_{\theta(e)} &= -\frac{T_e}{|q|B_0}\frac{d}{dr}\log n_0\left(r\right) \\ v_{z(e)} &= u_0 \\ v_{r(e)} &= 0. \end{aligned} \tag{16}$$

Similarly, we find following equation for the fluctuations in potential:

$$\frac{d^2\tilde{\phi}}{dr^2} + \left(\frac{1}{r} - \frac{2r}{r_0^2}\right)\frac{d\tilde{\phi}}{dr} + \left(Q - \frac{m^2}{r^2}\right)\tilde{\phi} = 0, \tag{17}$$

where Q is a constant given by

$$Q = \frac{1}{\rho^2\left(\omega + i\nu_i\right)}\left(\omega^* - \frac{\omega\left(\omega^* + i\nu_{||}\right)}{\omega - \omega_1 + i\nu_{||}}\right). \tag{18}$$

Here, the quantities are defined as

$$\begin{aligned} \rho &= c_s/\Omega_i \\ \omega^* &= -\frac{T_e}{|q|B_0}\frac{m}{r}\frac{1}{n_0}\frac{dn_0}{dr} \\ \nu_{||} &= \frac{k_z^2 T_e}{m_e \nu_e} \\ \omega_1 &= k_z u_0. \end{aligned}$$

Eq. 17 is a second-order ODE that yields the radial dependence of the plasma potential. In order to numerically solve this equation and compare it with our experimental observations, we adopted the following method. First, we approximated the background density n_0 as Gaussian by fitting a profile to the mean light intensity profile exhibited in Fig. 8. Second, we chose a value for ω, substituted the numerical fit for the background density into Eq. 18 and solved for Q . Third, we implemented this value for Q in Eq. 17, set $\phi\left(0\right) = 0$ and $\phi'\left(0\right) \approx 0$ as initial conditions, and numerically integrated the equation to the experimentally observed bound in Fig. 8: $\phi\left(r = 0.4r_c\right)$. Finally, we iterated the value of the frequency ω until the solution at $r = 0.4r_c$ converged to zero. In this way we were able to determine both the real part of the frequency and the imaginary part, i.e. the growth rate for a profile that qualitatively resembles the experimental result.

For the physical constants in Eqs. 17 and 18, we employed typical values for the H6MS centerline at the thruster face, which are summarized in Table 1. For the wave components in the azimuthal and parallel direction, we assumed the mode was $m = 1$ to be consistent with the experimental observations, and since we could not measure k_z directly with our experimental setup, we allowed this to be free parameter. Following this method, we show in Fig. 11 the real component of the frequency and the growth rate as functions of the parallel wavenumber.

From the growth rate, we note that for all values of parallel wavenumber, the modes are unstable. This suggests that for any parallel wavenumber plotted, an $m = 1$ azimuthal mode can be driven by the existing density gradient. Since all of these investigated values for the wavenumber are allowed by the model assumptions $\omega/k_z \gg c_s$, the actual value of the parallel wave component in the thruster is likely dictated by characteristic lengths in the axial direction, e.g. the length scale of the density gradient. Assuming this is on the order of several channel lengths, this suggests $k_z \geq 15$ m^{-1} are reasonable values for the parallel wave vector. From the left hand side of Fig. 11, we can see that in this range of realistic wave vectors, the real

Parameter	Value
T_e	2 eV
ν_i	10^4 s^{-1}
ν_e	6×10^7 s^{-1}
u_0	25 km/s
B_0	250 G
r_0	$0.06\mathrm{r}_c$

Table 1. Centerline H6MS parameters employed in the two-fluid drift model.

component of the frequency exhibits a maximum absolute value at -50 kHz. According to our convention, this negative frequency corresponds to propagation in the clockwise direction, i.e. in the experimentally observed direction. Moreover, the value of the frequency is within a factor of two of the experimentally observed values (75 -90 kHz) reported in the previous section.

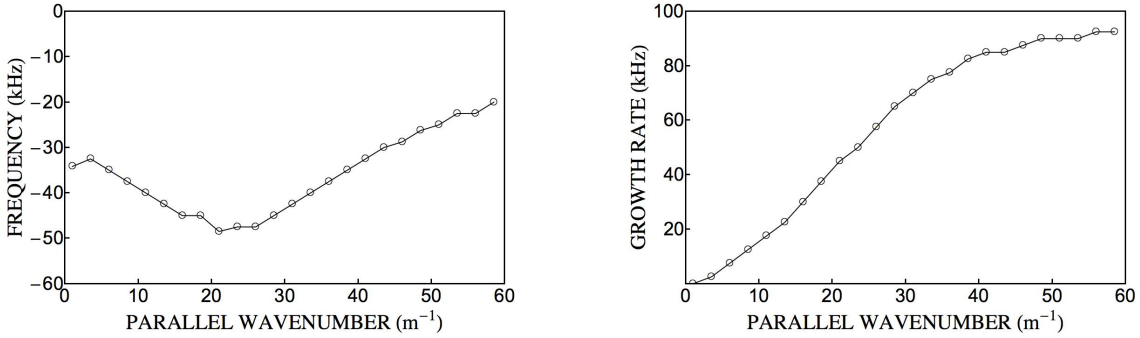

Figure 11. The calculated real component of the frequency and the growth rate for an $m = 1$ mode subject to the physical parameters in Table 1.

We thus conclude that based on the cathode parameters and subject to the assumptions we outlined above, the density gradient can drive an unstable mode close to the experimentally-observed frequency and with the right azimuthal character. As a further check of this simulation, we examine two quantities for the -50 kHz case, which we select since it is close to our experimentally observed frequency. First, we show in Fig. 12 the calculated square of the amplitude of the potential $|\tilde{\phi}(r)|^2$ as a function of radial position. We also plot the numerical fit to the light intensity profile we employed for our numerical simulation as an estimate for the background plasma density. Considering that subject to our low-frequency electrostatic assumption, $\tilde{\phi} \sim \tilde{n}/n_0$, it is evident from comparing our numerical result to Fig. 8 that the numerical simulation correctly captures the trend in amplitude. On the other hand, the peak of the modeled amplitude is shifted to the left as compared to the experimentally observed value. Similar discrepancies occurred in work by Ellis,[48] and it was suggested that these could result from oversimplification in the model (neglecting temperature gradients and electric field) or that the actual density profile deviates from Gaussian. It is also possible that our assumption that the mean intensity from the image is a proxy for the background density is invalid.

As a second check, we plot the phase of the numerical solution $\phi_\omega = \tan^{-1}\left[\mathrm{Re}\left(\phi(r)\, e^{im\theta}\right)/\mathrm{Im}\left(\phi(r)\, e^{im\theta}\right)\right]$ as a function of angle and radius in Fig. 13. Since the experimental calculations are subject to an arbitrary phase offset, we have rotated the numerical image by a constant to line up with the experimentally observed plot. Comparing this result with Fig. 10, we can see that the numerical simulation captures the radial component of propagation as well as the azimuthal character. The simulation does not lose coherency as the experimental result does with increasing radius. However, we note that the assumptions of the model break down with increasing radius such that we no longer expect the simulation to be predictive at these greater values. There are also some deviations in the character of the swirl between the two simulations, but ultimately, the model reflects the experimentally-observed behavior.

This phase-plot taken in conjunction with the qualitative agreement in amplitude dependence and mode

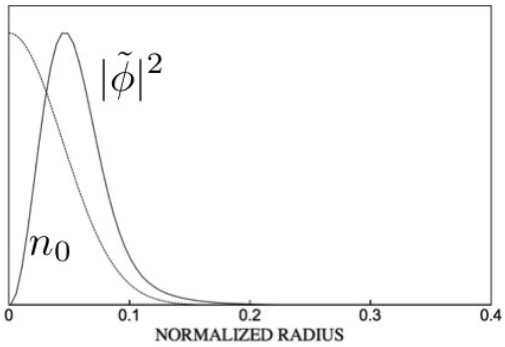

Figure 12. Amplitude predicted by the simplified model for cathode oscillations at -50 kHz with $k_z = 25$ m^{-1}. The normalized density profile employed in the model is also shown.

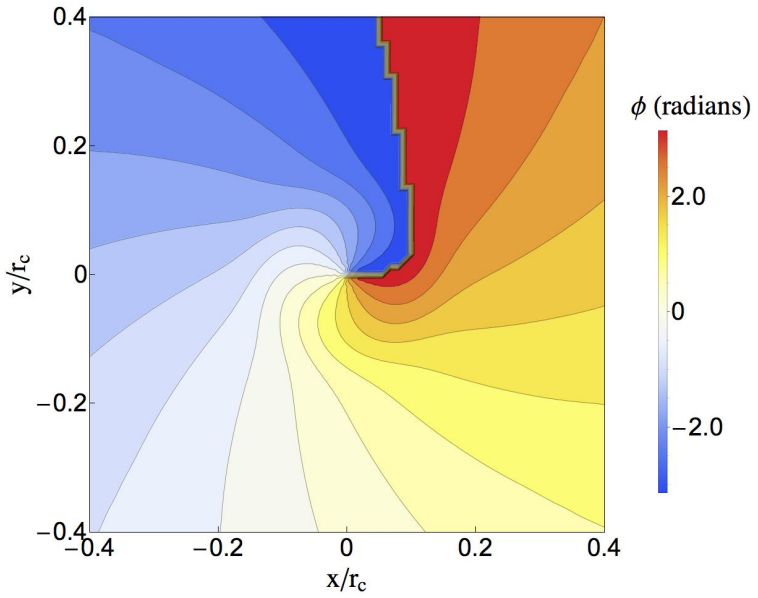

Figure 13. The theoretically predicted phase dependence for cathode oscillations at -50 kHz with $k_z = 25$ m^{-1}. The plot is only shown to the bounds of where the experimentally observed oscillation occurred.

frequency lend support to the argument that the propagating mode near the cathode is a high frequency, gradient-driven drift wave. This is a significant result since gradient-driven modes have been shown to contribute to cross-field transport,[48] and the presence of such a wave in the vicinity of the cathode suggests that this may be a mechanism in the MS configuration for electrons to cross field lines from the cathode into the channel.

As a final note, we mention here that although the cathodes and cathode plasmas are similar between the H6MS and H6US configurations, this mode has not been reported for the H6US–either through Fourier analysis of the discharge current or FASTcam imaging of the thruster face. Lower frequency (10 - 40 kHz) azimuthal modes that propagated in the channel were observed to extend[39]—in some cases—toward the cathode, but the difference in frequency, the fact that our observed mode did not propagate azimuthally in the channel, and the observation that the low-frequency waves in the H6US propagated in the opposite direction as our observed mode suggest that these are different phenomena.

This absence of a high frequency mode in the H6US is a surprising result given the relative similarities between plasma conditions at the cathode. With that said, the discrepancy as indicated by FASTcam results from H6US testing might be explained in light of the fact that high speed imaging never probed frequencies as high as 80 kHz. It therefore is possible that the mode persists in the H6US but has yet to be measured with a diagnostic with sufficient bandwidth. On the other hand, even if the mode simply was above the

frequency range of the H6US diagnostics, the discrepancy between the observation of the mode in the H6MS discharge current and its absence in the H6US analysis has yet to be resolved.

C. Absence of spokes

While in the previous sections, we have attempted to identify the character of the propagating modes we observed in the MS and to compare them to the US configuration, in this final section we devote a brief discussion to the conspicuous absence of a low-frequency azimuthal oscillation in the channel region. This absence is in direct contrast to observations of the H6US configuration where low-frequency azimuthal oscillations denoted as "rotating spokes" with $m \geq 1$ were identified in the frequency range from 10 - 40 kHz under a number of different operating conditions[37,38] including the nominal one reported here.[41]

While we recognize that the analysis we have performed here may not be sufficiently sensitive to exhibit a high enough signal to noise ratio to detect these oscillations, our results do reveal that any azimuthal oscillation in this frequency range is orders of magnitude lower than the exhibited frequencies at 8 kHz and 75-95 kHz. This is in direct contrast to results for the H6US where it was revealed that the spoke amplitudes could be comparable to the breathing mode amplitude. Significantly, rotating spokes have been speculated to play a critical role as a driving mechanism for the underlying physics in unshielded thrusters—responsible for 50% of the electron current.[18,37] However, we note that despite the fact that spokes do not appear in our observations of the H6MS, the thruster exhibits remarkably similar performance parameters to the H6US.[5] Spokes therefore do not seem to be a significant contributor to H6MS operation despite its comparable performance to the unshielded thruster.

V. Conclusion

In this investigation we have performed a characterization of the low-frequency oscillations (0 - 100 kHz) in a magnetically-shielded 6-kW hall thruster. The primary diagnostic we employed was a fast camera imaging system complemented by a translating single ion saturation probe. With these diagnostics and a series of post-processing steps, we have observed that at the nominal conditions of 300 V and 20 mg/s, the H6MS is characterized by two modes: a low-frequency oscillation at 8 kHz and a high frequency oscillation in the range $75 - 90$ kHz. Through a spatial analysis of these modes, we have found that the low-frequency mode is relatively uniform across the thruster face with a drop in intensity at the centerline while the higher frequency component is localized near the cathode with a non-monotonic radial profile. A correlation analysis of these modes revealed that the low frequency wave has a global character with no azimuthal dependence and the higher frequency component is an $m = 1$ mode with a radial component of propagation.

With the results from our experimental characterization, we have performed a theoretical analysis of the two modes and where appropriate compared our results with previous observations of the unshielded configuration H6US. We have identified the lower frequency, global wave as an example of the classic breathing mode oscillation and offered an explanation for the discrepancy in the frequency of this mode as compared to the frequency of the breathing mode in the H6US based on the differing lengths for their characterization ionization zones. For the oscillations near the cathode, we have implemented a simple cylindrical model for gradient-driven instabilities in the region of the cathode and arrived at solution with a comparable frequency and spatial character to the observed mode. This result suggests that the frequency at the centerline of the thruster may be largely gradient-driven. While a comparable cathode oscillation was not reported for the H6US, the frequency of this mode was beyond the range of the diagnostic employed in these tests. Given the similarity between the cathode plasmas in the two configurations, we have postulated that it is possible that this mode does in fact exist in the H6US. As a last consideration, we have noted that in direct contrast to results from the H6US experiments under the same operating conditions, the H6MS did not exhibit any spoke-like oscillations in the channel. The theoretical foundation as to why the instability occurs in H6US and not the H6US remains unclear; however, we have found the significant result that despite the absence of the spoke, the H6MS exhibits comparable performance parameters to the H6US. This suggests the spoke has a minimal role to play in the underlying physics of the H6MS.

Through a set of experimental trials and analytical arguments, we thus have characterized for the first time a number of oscillations in a magnetically shielded thruster. Our experimental results and our speculation as to the origin of the observed modes represent a necessary step toward both guiding improved simulations of MS thrusters and revealing the underlying processes governing thruster operation.

Acknowledgments

The research described in this paper was carried out at the Jet Propulsion Laboratory, California Institute of Technology, under a contract with the National Aeronautics and Space Administration and funded through the In-Space Propulsion Technologies program. The authors would like to acknowledge Ray Swindlehurst and Nowell Niblitt for their assistance in running the experimental facility. We are also grateful to Dr. Dan Goebel and Dr. Ioannis Mikellides for providing data on the H6MS configuration and to Michael Sekerak for his assistance in understanding the FASTcam algorithms developed at the University of Michigan.

References

[1]Mikellides, I. G., Katz, I., Hofer, R. R., and Goebel, D. M., "Magnetic shielding of walls from the unmagnetized ion beam in a Hall thruster," *Applied Physics Letters*, Vol. 102, No. 2, 2013, pp. 023509.

[2]DeGyrs, K., Mathers, A., Welander, B., and Khayms, V., "Demonstration of 10,400 Hours of Operation on a 4.5 kW Qualification Model Hall Thruster," *46st Joint Propulsion Conference, Nashville, TN, July 25-28, 2010, AIAA-2010-6698.*, 2010.

[3]Mikellides, I. G., Katz, I., Hofer, R. R., Goebel, D. M., de Grys, K., and Mathers, A., "Magnetic shielding of the channel walls in a Hall plasma accelerator," *Physics of Plasmas*, Vol. 18, No. 3, 2011, pp. 033501.

[4]Mikellides, I., Katz, I., and Hofer, R., "Design of a Laboratory Hall Thruster with Magnetically Shielded Channel Walls, Phase I: Numerical Simulations," *47th AIAA/ASME/SAE/ASEE Joint Propulsion Conference & Exhibit*, Joint Propulsion Conferences, American Institute of Aeronautics and Astronautics, July 2011.

[5]Hofer, R., Goebel, D., Mikellides, I., and Katz, I., "Design of a Laboratory Hall Thruster with Magnetically Shielded Channel Walls, Phase II: Experiments," *48th AIAA/ASME/SAE/ASEE Joint Propulsion Conference & Exhibit*, Joint Propulsion Conferences, American Institute of Aeronautics and Astronautics, July 2012.

[6]Mikellides, I., Katz, I., Hofer, R., and Goebel, D., "Design of a Laboratory Hall Thruster with Magnetically Shielded Channel Walls, Phase III: Comparison of Theory with Experiment," *48th AIAA/ASME/SAE/ASEE Joint Propulsion Conference & Exhibit*, Joint Propulsion Conferences, American Institute of Aeronautics and Astronautics, July 2012.

[7]Mikellides, I., Katz, I., Hofer, R., Goebel, D., de Grys, K., and Mathers, A., "Magnetic Shielding of the Acceleration Channel Walls in a Long-Life Hall Thruster," *46th AIAA/ASME/SAE/ASEE Joint Propulsion Conference & Exhibit*, Joint Propulsion Conferences, American Institute of Aeronautics and Astronautics, July 2010.

[8]Goebel, D. M., Jameson, K. K., Katz, I., and Mikellides, I. G., "Potential fluctuations and energetic ion production in hollow cathode discharges," *Physics of Plasmas*, Vol. 14, No. 10, 2007, pp. 103508.

[9]Mikellides, I. G., Katz, I., Goebel, D. M., Jameson, K. K., and Polk, J. E., "Wear Mechanisms in Electron Sources for Ion Propulsion, II: Discharge Hollow Cathode," *Journal of Propulsion and Power*, Vol. 24, No. 4, July 2008, pp. 866–879.

[10]Farnell, C. C., Williams, J. D., and Farnell, C. C., "Comparison of hollow cathode discharge plasma configurations," *Plasma Sources Science and Technology*, Vol. 20, No. 2, 2011, pp. 025006.

[11]Janes, G. S. and Lowder, R. S., "Anomalous Electron Diffusion and Ion Acceleration in a Low-Density Plasma," *Physics of Fluids*, Vol. 9, No. 6, 1966, pp. 1115–1123.

[12]Esipchuk, Y. and Tilinin, G., "Drift instability in a Hall-current plasma accelerator." *Sov. Physics-Tech. Physics*, Vol. 21, No. 4, 1976, pp. 013503.

[13]Meezan, N. B., Hargus, W. A., and Cappelli, M. A., "Anomalous electron mobility in a coaxial Hall discharge plasma," *Phys. Rev. E*, Vol. 63, Jan 2001, pp. 026410.

[14]Lazurenko, A., Coduti, G., Mazouffre, S., and Bonhomme, G., "Dispersion relation of high-frequency plasma oscillations in Hall thrusters," *Physics of Plasmas*, Vol. 15, No. 3, 2008, pp. 034502.

[15]Adam, J. C., Heron, A., and Laval, G., "Study of stationary plasma thrusters using two-dimensional fully kinetic simulations," *Physics of Plasmas*, Vol. 11, No. 1, 2004, pp. 295–305.

[16]Perez-Luna, J., Hagelaar, G., Garrigues, L., Debuit, N., and Boeuf, J., "Influence of azimuthal instabilities on electron motion in a Hall Effect Thruster," *30th International Electric Propulsion Conference, Florence, Italy September 17-20, 2007 IEPC-2007-124*, 2007.

[17]McDonald, M. S. and Gallimore, A. D., "Rotating Spoke Instabilities in Hall Thrusters," *Plasma Science, IEEE Transactions on*, Vol. 39, No. 11, 2011, pp. 2952–2953.

[18]Ellison, C. L., Raitses, Y., and Fisch, N. J., "Cross-field electron transport induced by a rotating spoke in a cylindrical Hall thruster," *Physics of Plasmas*, Vol. 19, No. 1, 2012, pp. 013503.

[19]Brophy, J., Friedman, L., Culick, F., et al., "Asteroid Retrieval Feasibility Study," *Keck Institute for Space Studies, Califonia Institute of Technology, Jet Propulsion Laboratory*, 2012.

[20]Boeuf, J. P. and Garrigues, L., "Low frequency oscillations in a stationary plasma thruster," *Journal of Applied Physics*, Vol. 84, No. 7, 1998, pp. 3541–3554.

[21]Schmidt, D. P., Meezan, N. B., Jr, W. A. H., and Cappelli, M. A., "A low-power, linear-geometry Hall plasma source with an open electron-drift," *Plasma Sources Science and Technology*, Vol. 9, No. 1, 2000, pp. 68.

[22]Chesta, E., Lam, C. M., Meezan, N. B., Schmidt, D. P., and Cappelli, M. A., "A characterization of plasma fluctuations within a Hall discharge," *Plasma Science, IEEE Transactions on*, Vol. 29, No. 4, 2001, pp. 582–591.

[23]Lobbia, R. and Gallimore, A., "Two-dimensional Time-resolved Breathing Mode Plasma Fluctuation Variation with Hall Thruster Discharge Settings," *31st International Electric Propulsion Conference, Ann Arbor, MI, USA, September 20-24, 2009, IEPC-2009-106*, 2009.

[24]Choueiri, E. Y., "Plasma oscillations in Hall thrusters," *Physics of Plasmas*, Vol. 8, No. 4, 2001, pp. 1411–1426.

[25]Haas, J. M., Hofer, R. R., Brown, D. L., Reid, B. M., and Gallimore, A. D., "Design of the H6 Hall Thruster for High Thrust/Power Investigation," *54th JANNAF Propulsion Meeting, Denver, CO, May 14-17, 2007*, 2007.

[26]Brown, D., Reid, B., Gallimore, A., Hofer, R., Haas, J., and Larson, C., "Performance Characterization and Design Verification of the H6 Laboratory Model Hall Thruster," *54th JANNAF Propulsion Meeting, Denver, CO, May 14-17, 2007*, 2007.

[27]Reid, B., Gallimore, A., Hofer, R., Li, Y., and Haas, J., "Anode Design and Verification for the H6 Hall Thruster," *54th JANNAF Propulsion Meeting, Denver, CO, May 14-17, 2007*, 2007.

[28]Hofer, R., Goebel, D., and Watkins, R., "Compact LaB6 Hollow Cathode for a 6 kW Laboratory Hall Thruster," *54th JANNAF Propulsion Meeting, Denver, CO, May 14-17, 2007*, 2007.

[29]Huang, W., Gallimore, A., and Hofer, R., "Neutral Flow Evolution in a 6-kW Hall Thruster," *Journal of Propulsion and Power*, Vol. 27, 2011, pp. 553–563.

[30]Goebel, D., Jameson, K., and Hofer, R., "Hall Thruster Cathode Flow Impact on Coupling Voltage and Cathode Life," *Journal of Propulsion and Power*, Vol. 28, 2012, pp. 355–363.

[31]Goebel, D. M. and Watkins, R. M., "Compact lanthanum hexaboride hollow cathode," *Review of Scientific Instruments*, Vol. 81, No. 8, 2010, pp. 083504.

[32]Morozov, A., Espichuk, Y., Kapulkin, A., Nevroskii, V., and Smirno, V., "Effect of the magnetic field on a closed-electron-drift accelerator," *Sov. Phys. Tech. Phys.*, Vol. 17, No. 3, 1972, pp. 482–487.

[33]Gascon, N. and Cappelli, M., "Plasma instabilities in the ionization regime of a Hall thruster," *39th AIAA/ASME/SAE/ASEE Joint Propulsion Conference and Exhibit, Huntsville, AL, July 20-23, 2003. AIAA-2003-4857.*, 2003.

[34]Escobar, E. and Ahedo, E., "Low-frequency azimuthal stability analysis of Hall thrusters," *48th AIAA/ASME/SAE/ASEE Joint Propulsion Conference and Exhibit*, No. AIAA 2012-4180, 2012.

[35]Frias, W., Smolyakov, A. I., Kaganovich, I. D., and Raitses, Y., "Long wavelength gradient drift instability in Hall plasma devices. I. Fluid theory," *Physics of Plasmas*, Vol. 19, No. 7, 2012, pp. 072112.

[36]Frias, W., Smolyakov, A. I., Kaganovich, I. D., and Raitses, Y., "Long wavelength gradient drift instability in Hall plasma devices. II. Applications," *Physics of Plasmas*, Vol. 20, No. 5, 2013, pp. 052108.

[37]McDonald, M. and Gallimore, A., "Measurement of Cross-Field Electron Current in a Hall Thruster Due to Rotating Spoke Instability," *47th AIAA/ASME/SAE/ASEE Joint Propulsion Conference & Exhibit, AIAA 2011-5810.*, 2011.

[38]McDonald, M. and Gallimore, A., "Parametric Investigation of the Rotating Spoke Instability in Hall Thruster," *32nd International Electric Propulsion Conference, Wiesbaden, Germany. IEPC 2011-242*, 2011.

[39]McDonald, M., *Electron Transport in Hall Thrusters, Ph.D Thesis*, Ph.D Thesis, University of Michigan, Princeton, NJ, 2012.

[40]Sekerak, M., McDonald, M., Hofer, R., and Gallimore, A., "Hall Thruster Plume Measurements from High-Speed Dual Langmuir Probes with Ion Saturation Reference," *34th IEEE Aerospace Conference, Big Sky, MT, March 2-9, 2013. IEEE-2013-2129*, 2013.

[41]Sekerak, M., Longmier, B., Gallimore, A., Brown, D., Hofer, R., and Polk, J., "Mode Transitions in Hall Effect Thrusters," *49th AIAA/ASME/SAE/ASEE Joint Propulsion Conference and Exhibit, July 14-17, 2013, San Jose, CA.*, 2013.

[42]Darnon, F., Lyszyk, M., Bouchoule, A., Darnon, F., Lyszyk, M., and Bouchoule, A., "Optical investigation on plasma investigations of SPT thrusters," *33rd Joint Propulsion Conference and Exhibit*, Joint Propulsion Conferences, American Institute of Aeronautics and Astronautics, July 1997.

[43]Ellison, C., Raitses, Y., and Fisch, N., "Fast Camera Imaging of Hall Thruster Ignition," *Plasma Science, IEEE Transactions on*, Vol. 39, No. 11, 2011, pp. 2950–2951.

[44]Liu, D., Huffman, R. E., Branam, R. D., and Hargus, W. A., "Ultrahigh-speed imaging of hall-thruster discharge oscillations with krypton propellant," *Plasma Science, IEEE Transactions on*, Vol. 39, No. 11, 2011, pp. 2926–2927.

[45]Barral, S. and Ahedo, E., "On the Origin of Low Frequency Oscillations in Hall Thrusters," *AIP Conference Proceedings*, Vol. 993, No. 1, 2008, pp. 439–442.

[46]Barral, S. and Ahedo, E., "Low-frequency model of breathing oscillations in Hall discharges," *Phys. Rev. E*, Vol. 79, Apr 2009, pp. 046401.

[47]Fife, J., Martinez-Sanchez, M., Szabo, J., Fife, J., Martinez-Sanchez, M., and Szabo, J., "A numerical study of low-frequency discharge oscillations in Hall thrusters," *33rd Joint Propulsion Conference and Exhibit*, Joint Propulsion Conferences, American Institute of Aeronautics and Astronautics, July 1997.

[48]Ellis, R. F., Marden-Marshall, E., and Majeski, R., "Collisional drift instability of a weakly ionized argon plasma," *Plasma Physics*, Vol. 22, No. 2, 1980, pp. 113.